






Resolved observations at 31 GHz of spinning dust emissivity variations in ρ Oph

Carla Arce-Tord ¹★, Matias Vidal ²★, Simon Casassus ¹★, Miguel Cárcamo,^{3,4}
Clive Dickinson ⁴, Brandon S. Hensley,⁵† Ricardo Génova-Santos,^{6,7}
J. Richard Bond,⁸ Michael E. Jones ⁹, Anthony C. S. Readhead,¹⁰
Angela C. Taylor⁹ and J. Anton Zensus¹¹

¹Departamento de Astronomía, Universidad de Chile, Camino El Observatorio 1515, Las Condes, Santiago, Chile

²Facultad de Ingeniería, Núcleo de Astroquímica & Astrofísica, Universidad Autónoma de Chile, Av. Pedro de Valdivia 425, Providencia, Santiago, Chile

³Departamento de Ingeniería Informática, Universidad de Santiago de Chile, Av. Ecuador, 3659, Santiago, Chile

⁴Department of Physics and Astronomy, School of Natural Sciences, Jodrell Bank Centre for Astrophysics, Alan Turing Building, The University of Manchester, Oxford Road, Manchester, M13 9PL, UK

⁵Department of Astrophysical Sciences, Princeton University, Princeton, NJ 08544, USA

⁶Instituto de Astrofísica de Canarias, E-38200 La Laguna, Tenerife, Canary Islands, Spain

⁷Departamento de Astrofísica, Universidad de La Laguna (ULL), E-38206 La Laguna, Tenerife, Spain

⁸Canadian Institute for Theoretical Astrophysics, University of Toronto, 60 St George Street, Toronto, ON, M5S 3H8, Canada

⁹Sub-department of Astrophysics, University of Oxford, Denys Wilkinson Building, Keble Road, Oxford OX1 3RH, UK

¹⁰Cahill Centre for Astronomy and Astrophysics, California Institute of Technology, Pasadena, CA 91125, USA

¹¹Max-Planck-Institut für Radioastronomie, Postfach 2024, D-53010 Bonn, Germany

Accepted 2020 May 18. Received 2020 May 17; in original form 2019 October 13

ABSTRACT

The ρ Oph molecular cloud is one of the best examples of spinning dust emission, first detected by the cosmic background imager (CBI). Here, we present 4.5 arcmin observations with CBI 2 that confirm 31 GHz emission from ρ Oph W, the PDR exposed to B-type star HD 147889, and highlight the absence of signal from S1, the brightest IR nebula in the complex. In order to quantify an association with dust-related emission mechanisms, we calculated correlations at different angular resolutions between the 31 GHz map and proxies for the column density of IR emitters, dust radiance, and optical depth templates. We found that the 31 GHz emission correlates best with the PAH column density tracers, while the correlation with the dust radiance improves when considering emission that is more extended (from the shorter baselines), suggesting that the angular resolution of the observations affects the correlation results. A proxy for the spinning dust emissivity reveals large variations within the complex, with a dynamic range of 25 at 3σ and a variation by a factor of at least 23, at 3σ , between the peak in ρ Oph W and the location of S1, which means that environmental factors are responsible for boosting spinning dust emissivities locally.

Key words: radiation mechanisms: general – ISM: clouds – dust, extinction – ISM: individual objects: ρ Oph – photodissociation region – radio continuum: ISM.

1 INTRODUCTION

Since 1996, experiments designed to measure CMB anisotropies have found a diffuse foreground in certain regions of our Galaxy in the range of 10–60 GHz. For instance, the *Cosmic Background Explorer* satellite measured a statistical correlation between the

emission at 31.5 GHz and 140 μ m, at high Galactic latitudes and over large angular scales (Kogut et al. 1996). The spectral index of this radio-IR correlated signal was explained by a superposition of dust and free-free emission. Later, Leitch et al. (1997) detected diffuse emission at 14.5 GHz, which was spatially correlated with IRAS 100 μ m. This emission was 60 times stronger than the free-free emission and well in excess of the predicted levels from synchrotron and Rayleigh-Jeans dust emission, thus confirming the existence of an anomalous microwave emission (AME).

The AME is a dust-correlated signal observed in the 10–100 GHz frequency range (see Dickinson et al. 2018 for a review). Numerous

* E-mail: carce@das.uchile.cl (CA-T); matias.vidal@uautonoma.cl (MV); simon@das.uchile.cl (SC)

† Spitzer Fellow

detections have been made in our Galaxy by separating the AME excess from the other radio components, namely synchrotron, free-free, CMB, and thermal dust emission. It has been distinctly measured by CMB experiments and telescopes at angular resolutions of $\sim 1^\circ$; for instance, the WMAP (Bennett et al. 2013) and *Planck* (Planck Collaboration XII 2013; Planck Collaboration XII 2014b) satellites have provided detailed information on diffuse emission mechanisms in the Galaxy through full-sky maps. Based on such surveys, AME accounts for ≈ 30 per cent of the Galactic diffuse emission at 30 GHz (Planck Collaboration XII 2014b). AME has also been observed in several clouds and H II regions (e.g. Finkbeiner 2004; Watson et al. 2005; Casassus et al. 2006; Davies et al. 2006, Dickinson et al. 2007, 2009, Ami Consortium 2009; Planck Collaboration 2011; Vidal et al. 2011; Planck Collaboration XV 2014c; Génova-Santos et al. 2015), some of them being arcminute resolution observations of well-known regions (Casassus et al. 2008; Scaife et al. 2010a; Castellanos et al. 2011; Tibbs et al. 2011; Battistelli et al. 2015). There have been a few extra-galactic AME detections as well, such as in the galaxy NGC 6946 (Murphy et al. 2010a; Scaife et al. 2010b; Hensley, Murphy & Staguhn 2015; Murphy et al. 2018) and M 31 (Planck Collaboration XXV 2015; Battistelli et al. 2019), although extra-galactic studies are still a challenge due to the diffuse nature of the emission.

AME is thought to originate from dust grains rotating at GHz frequencies and emitting as electric dipoles. Long before its detection, Erickson (1957) proposed that electric dipole emission from spinning dust (SD) grains could produce non-thermal radio emission. Draine & Lazarian (1998a) calculated that interstellar spinning grains can produce emission in the range from 10 to 100 GHz, at levels that could account for the AME. Since then, additional detailed theoretical models have been constructed to calculate the SD emission, taking into account all the known physical mechanisms that affect the rotation of the grains. The observed spectral energy distributions of a number of detections are a qualitative match to SD models (e.g. Planck Collaboration XV 2014c). Thus, the SD hypothesis has been the most accepted to describe the nature of the AME.

As SD emission depends on the environmental conditions, a quantitative comparison between AME observations and synthetic spectra can give us information on the local physical parameters. However, even when there is a dependence on the environmental parameters, variations over a wide range of environmental conditions (e.g. typical conditions for a dark cloud versus a photodissociation region) only produce emissivity changes smaller than an order of magnitude (e.g. Draine & Lazarian 1998b; Ali-Haïmoud, Hirata & Dickinson 2009). Although greater changes in SD emissivity models are observed by varying parameters intrinsic to the grain population, as shown by Hensley & Draine (2017a), where they highlighted the importance of grain size, electric dipole, and grain charge distributions. Observationally, Tibbs et al. (2016) and Vidal et al. (2020) reported that they can only explain SD emissivity variations in different clouds by modifying the grain size distribution for the smallest grains.

Within the SD model, the smallest grains are the largest contributors to the emission. These have sub-nanometer sizes and spin at GHz frequencies. Polycyclic aromatic hydrocarbons (PAHs) are natural candidates for the AME carriers, as they are a well-established nanometric-sized dust population (Tielens 2008), and correlations between AME and PAHs tracers have been observed (Ysard, Miville-Deschênes & Verstraete 2010; Scaife et al. 2010a; Tibbs et al. 2011; Battistelli et al. 2015). However, a full-sky study by Hensley, Draine & Meisner (2016) found a lack of

correlation between the *Planck* AME map and a template of PAH emission constructed with 12 μm data. Tibbs et al. (2013) found that in Perseus Very Small Grains (VSGs) emission at 24 μm is more correlated with AME than 5.8 μm and 8 μm PAH templates. Recently, Vidal et al. (2020) confirmed that 30 GHz AME from the translucent cloud LDN 1780 correlates better with a 70 μm map. Rotational nanosilicates have also been considered as the carriers of the AME and they can account for all the emission without the need of PAHs (Hoang, Vinh & Quynh Lan 2016; Hensley & Draine 2017b). These results have raised questions about the PAHs hypothesis as the unique carriers of AME.

One of the key characteristics of AME, based on observations, is that it seems to be always connected with photodissociation regions (PDRs). PDRs are optimal environments for SD production (Dickinson et al. 2018): there is high density gas, presence of charged PAHs and a moderate interstellar radiation field (ISRF) that favours an abundance of small particles due to the destruction of large grains. For instance, Pilleri et al. (2012) fitted *ISO* mid-IR spectra and showed that an increasing UV-radiation field in PDRs favours grains destruction. Also, Habart et al. (2003) used *ISO* observations and concluded that the emission in the ρ Oph W PDR is dominated by the photoelectric heating from PAHs and VSGs. The most significant AME detections have been traced back to PDRs (Casassus et al. 2008; Planck Collaboration 2011; Vidal et al. 2020).

Among the most convincing observations on the SD hypothesis is the ρ Ophiuchi (ρ Oph) molecular cloud, an intermediate-mass star-forming region and one of the brightest AME sources in the sky (Casassus et al. 2008; Planck Collaboration 2011). The region of ρ Oph exposed to UV radiation from HD 147889, the earliest-type star in the complex, forms a filamentary PDR whose brightest regions in the IR include the ρ Oph W PDR (Liseau et al. 1999; Habart et al. 2003). ρ Oph W is the nearest example of a PDR, at a distance of 134.3 ± 1.2 pc in the Gould Belt (Gaia Collaboration 2018). In radio-frequencies, observations with the cosmic background imager (CBI) by Casassus et al. (2008) showed that the bright cm-wave continuum from ρ Oph, for a total WMAP 33 GHz flux density of ~ 20 Jy, stems from ρ Oph W and is fitted by SD models. They found that the bulk of the emission does not originate from the most conspicuous IR source, S1. This motivated the study of variations of the SD emissivity per H-nucleus, $j_v = I_v/N_H$, which at the angular resolutions of their observations led to the tentative detection of j_v .

In this work, we report CBI 2 observations of ρ Oph W, at a frequency of 31 GHz and an angular resolution of 4.5 arcmin. In relation to the CBI, this new data set provides a finer angular resolution by a factor of 1.5 and better surface brightness sensitivity. Section 2 of this paper describes the CBI2 characteristics and observations, as well as the ancillary data. Section 3 presents a qualitative analysis of the IR/radio features of the PDR. In Section 4, we describe the results of the correlation analysis between the 31 GHz data and the different IR and column density templates, and in Section 5 we analyse the size variations of the PAHs in the PDR. In Section 6, we quantify the SD emissivity variations throughout ρ Oph and discuss the implications of our results, and in Section 7 we conclude.

2 THE DATA

2.1 Cosmic background imager 2 observations

The observations at 31 GHz were carried out with the CBI2, an interferometer composed of 13 Cassegrain antennas (Taylor et al.

Table 1. Technical specifications for the CBI and CBI2.

	CBI	CBI2
Years of operation	1999–2006	2006–2008
Observing frequencies (GHz)	26–36	26–36
Number of antennas	13	13
Number of channels (1 GHz)	10	10
Number of baselines	78	78
Antenna size (m)	0.9	1.4
Primary beam FWHM (arcmin)	45	28.2

Table 2. Coordinates for the observation of the ρ Oph W PDR and the pointings defined around it. S1 and SR3 are the early-type stars of interest. The angular resolution of the observation is 4.5 arcmin.

	RA ^a	Dec. ^b	RMS (mJy beam ⁻¹)
ρ Oph W PDR	16:25:57.0	−24:20:48.0	6.7
ρ Oph 1	16:26:06.0	−24:37:51.0	9.3
ρ Oph 2	16:26:00.0	−24:22:32.0	30.2
ρ Oph 3	16:25:14.0	−24:11:39.0	15.0
ρ Oph S1	16:26:34.18	−24:23:28.33	12.7
ρ Oph SR3	16:26:09.32	−24:34:12.18	9.6

^aJ2000. Right ascensions are in HMS.

^bJ2000. Declinations are in DMS.

2011). The CBI2 is an upgraded version of the CBI (Padin et al. 2002). In 2006, the antennas were upgraded from 0.9 m (CBI) to 1.4 m dishes (CBI2). As opposed to the CBI, CBI2 has an increased surface brightness sensitivity at small angular scales due to the incorporation of larger dishes that provide a better filling factor for the array. Technical specifications of the CBI and CBI2 are presented in Table 1.

The observations were spread over 27 d in 2008 March. We acquired data distributed in six pointings: one pointing centred at the ρ Oph W PDR, three pointings defined around the PDR, and two more pointings centred at stars S1 and SR3. Table 2 shows the coordinates for each pointing, as well as their respective RMS noise. The data set was reduced using the standard CBI pipeline (CBICAL) and software (Pearson et al. 2003; Readhead et al. 2004a,b), with Jupiter as the main flux calibrator. As the CBI2 is a co-mounted interferometer, the pointing error associated with each antenna has to be accounted by the combined pointing error of the baseline pairs of antennas. This yields a residual pointing error of ~ 0.5 arcmin (Taylor et al. 2011).

2.2 Image reconstruction

We considered two approaches to reconstruct an image from the CBI2 data. One of them is the traditional `clean` algorithm, in which we used a *Briggs* robust 0 weighting scheme to construct a continuum mosaic. Fig. 1 shows the reconstructed mosaic using the CASA 5.1 `clean` task (McMullin et al. 2007). This mosaic shows the location of the three early-type stars in the field - HD 147889, S1 and SR3. It also presents the 31 GHz intensity contours at 3σ , 5σ , 10σ , 15σ , and 20σ , for an RMS noise of $\sigma \approx 0.01$ Jy beam⁻¹. The dashed circle represents the 28.2 arcmin primary beam of the central pointing (ρ Oph W PDR in Table 2), and the bottom left green ellipse shows the synthesized primary beam, with a size of 4.6×4.0 arcmin.

In a second approach, we used an alternative image reconstruction strategy, based on non-parametric image deconvolution, as in the maximum-entropy method (following the algorithms described in

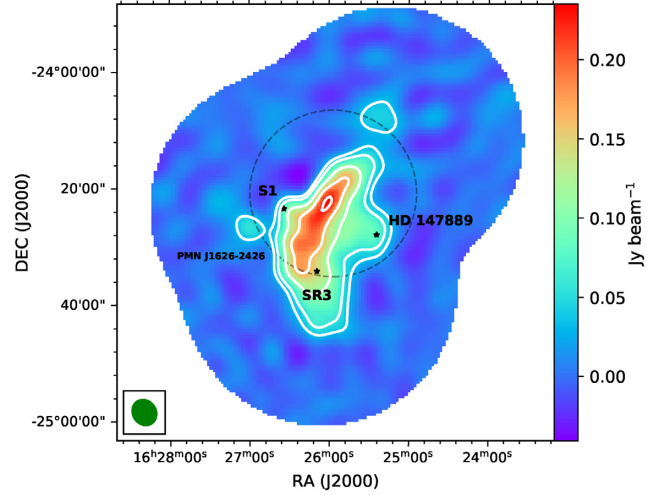


Figure 1. Mosaic of the 31 GHz continuum measured by CBI2 in units of Jy beam⁻¹. This image was reconstructed using the CASA `clean` task. The RMS noise is $\sigma \approx 0.01$ Jy beam⁻¹, and we show intensity contours for 3σ , 5σ , 10σ , 15σ , and 20σ . The star markers indicate the three early-type stars in the field: S1, SR3, and HD 147889. We also detected radio galaxy PMN J1626-2426 (labelled in the figure). The CBI2 synthesized beam (4.6×4.0 arcmin) is shown as a green ellipse on the bottom left and the primary beam for the main pointing (28.2 arcmin FWHM) is shown as a dashed circle.

Casassus et al. 2006, 2008). Here, we used the `gpu-uvmem` package (Cárcamo et al. 2018), implemented in GPU architectures. Because of entropy regularization and image positivity, the model image can superresolve the `clean` beam, in the sense that its effective angular resolution is $\sim 1/3$ that of the natural-weighted beam (so even finer than uniform weights). To obtain a model sky image that fits the data, we need to solve the usual deconvolution problem, i.e. obtain the model image I^m that minimizes a merit function L :

$$L = \chi^2 - \lambda \sum_i p_i \ln(p_i/M), \quad (1)$$

where

$$\chi^2 = \frac{1}{2} \sum_{k=0}^N \omega_k \|V_k^\circ - V_k^m\|^2. \quad (2)$$

Here, V_k° are the observed visibilities, each with weight ω_k , and V_k^m are the model visibilities calculated on the model images. The optimization is carried out by introducing the dimensionless free parameters $p_i = I_i/\sigma_D$, and M is the minimum value for the free parameters. In this case, we set $M = 10^{-3}$ and $\lambda = 2 \times 10^{-2}$. The `gpu-uvmem` algorithm also estimates a theoretical noise map as

$$\sigma = \sqrt{\frac{1}{\sum_{p=1}^P \bar{A}_p^2 / \hat{\sigma}^2}}, \quad (3)$$

where P is the number of pointings, $\bar{A}_p = \sum_{f=1}^F A_{v_f} / F$ is the mean of the primary beams over all frequencies $\{v_f\}_{f=1}^F$ available in pointing p , and $\hat{\sigma}$ is the noise on the dirty map using natural weights. Error propagation in the dirty map yields:

$$\hat{\sigma} = \sqrt{\frac{1}{\sum_k \omega_k}}. \quad (4)$$

Table 3. Flux densities and spectral indexes for source PMN J1626-2426, detected at RA 16:27:01.8, Dec. -24:26:33.7 (J2000). The spectral index follows the convention $S_\nu \propto \nu^\alpha$ and it was calculated between the 31 GHz flux from the `clean` map and the catalogued fluxes. The reported fluxes correspond to different epochs, indicating variability in the spectrum.

Observing Frequency (GHz)	Flux Density (mJy)	$\alpha_{(\nu/31 \text{ GHz})}$
1.4	57.2 ± 1.8^a	0.01 ± 0.03
4.8	132 ± 13^b	-0.43 ± 0.07
8.4	77.9^c	-0.21
20	78 ± 5^d	-0.61 ± 0.25
31	59.6 ± 5.3^e	–

^aReported in Condon et al. (1998).

^bReported in Griffith et al. (1994).

^cReported in Sowards-Emmerd et al. (2004). Error not reported.

^dReported in Murphy et al. (2010b).

^eReported in this work.

In order to avoid an underestimation of errors, we scaled the noise map so that its minimum value would match the RMS noise of the natural-weighted `clean` map. In increasing the noise level, we also included a correction for the number of correlated pixels in both maps, i.e. the noise in the `gpu-uvmem` model image is increased by $\sqrt{N_{\text{clean}}/N_{\text{uvmem}}} \sim 3$, where N_{clean} and N_{uvmem} are the number of pixels in each `clean` beam, and that of `gpu-uvmem` being ~ 3 times smaller than the natural-weight beam.

In our analysis, we used both the `clean` and `gpu-uvmem` maps. The `clean` map was used to measure the correlation of the 31 GHz emission with the IR templates and the proxies for PAHs. We did not use the `gpu-uvmem` map to perform the correlations as it has a variable angular resolution. Instead, as the `gpu-uvmem` map recovers the morphology of the 31 GHz emission in detail, we used it to construct an emissivity proxy to analyse the emissivity variations throughout the PDR.

In our reconstructed `clean` mosaic, we detected a point source located at RA 16:27:01.8, Dec. -24:26:33.7 (J2000) that corresponds to the radio galaxy PMN J1626-2426 (labelled in Fig. 1). This source is described in the PMN catalogue as a flat spectrum radio source, located at RA 16:27:00.01, Dec. 24:26:40.50 (J2000; Healey et al. 2007). In Table 3, we report the flux and spectral index ($S_\nu \propto \nu^\alpha$) of this point source at 31 GHz, along with catalogue measurements at other frequencies. We measured the flux at 31 GHz using aperture photometry with a circular aperture of radius 2.5 arcmin. It is interesting to point out that this source has a *Fermi* detection of 0.35 ± 0.04 pJy at 50 GeV (Nolan et al. 2012), observed during 2008 and 2010. Its radio spectrum shows variability, especially considering the flux difference between the 1.4 GHz data, observed during 1993, and the 4.8 GHz data, observed during 1990 (see Table 3). The 8.4 and 20 GHz data were taken during 2003 and 2006, respectively.

2.3 Ancillary data

The Wide-Field Infrared Survey Explorer (WISE) has surveyed the entire sky in four near-IR and mid-IR band-passes (Wright et al. 2010). Its near-IR survey at 3.4, 4.6, and 12 μm gives information on the emission from VSGs and PAHs in the interstellar medium. We worked with the 3.4 μm map, and the 12 μm processed map by Meisner & Finkbeiner (2014), who smoothed the data set to an angular resolution of 15 arcsec and removed the compact sources

Table 4. Summary of the ancillary data.

Instrument	Wavelength (μm)	Description
<i>Spitzer</i> –IRAC	8	Tracer for PAHs ^a .
WISE	3.4, 12	Tracer for PAHs ^a .
WISE	22	Tracer for VSGs.
<i>Spitzer</i> –MIPS	24	Tracer for VSGs.
<i>Herschel</i> –SPIRE	250	Tracer for big classical grains ^b

^aIn ρ Oph W, these bands are dominated by PAHs. The 3.4 μm map is a better tracer for the smallest PAHs.

^bGrains with sizes of \sim hundreds of nm in thermal equilibrium.

and optical artifacts from the image. We also used their map at 22 μm for comparison purposes.

Dust grain tracers were also obtained from the InfraRed Array Camera (IRAC) maps from the *Spitzer* Space Telescope survey. IRAC is a mid-IR camera with four channels at 3.6, 4.5, 5.8, and 8 μm (Fazio et al. 2004). In this case, we used the 8 μm template. The original data set is presented in units of MJy sr^{-1} and at an angular resolution of ~ 2 arcsec. We also used the 24 μm data set from the *Spitzer* Multiband Imaging Photometer (MIPS; Rieke et al. 2004). This photometer works at 24, 70 and 160 μm , producing maps with a native angular resolution between 6 and 40 arcsec.

In the particular case of ρ Oph W, both 8 and 12 μm bands are dominated by PAHs. Given the radiation field in HD 147 889 ($\chi \sim 400$, Habart et al. 2003) and for typical dust models (Draine & Li 2007; Compiègne et al. 2011), we expect both bands to be tracing primarily PAHs.

To study the thermal dust emission, we used data from the *Herschel* Gould Belt survey, which provides an extensive mapping of nearby molecular clouds, including detailed templates of ρ Oph (André et al. 2010; Pilbratt et al. 2010). Specifically, we used data from the Spectral Photometric Imaging Receiver (SPIRE), a three-band camera and spectrometer that works at 250, 350, and 500 μm (Griffin et al. 2010). We also worked with the dust temperature data set from the Photodetector Array Camera and Spectrometer (SPIRE–PACS), which has a native angular resolution of 36.3 arcsec (Ladjetate et al. 2020). A summary of our ancillary data is presented in Table 4.

3 QUALITATIVE RADIO/IR COMPARISONS

In Fig. 2, we compare the CBI 2 31 GHz emission reconstructed with the `gpu-uvmem` algorithm (Section 2.2) shown in contours, with the IRAC 8 μm in blue colour stretch, MIPS 24 μm in green, and SPIRE 250 μm in red. The 8 and 24 μm templates trace the emission of small hot grains (sub-nm and nm-sizes), while the 250 μm template traces thermal dust emission, mainly from big classical grains (size of hundreds of nm). In particular, the IRAC 8 μm template is a main tracer of PAHs in this region.

The black markers in Fig. 2 show the position of the three early-type stars in ρ Oph. S1 is a binary system composed of a B4V star and a K-type companion, with an effective temperature of $T_{\text{eff}} \approx 15\,800$ K. SR3, also known as Elia 2-16, is a B6V star with an effective temperature of $T_{\text{eff}} \approx 14\,000$ K. HD 147889, the main ionizing star of ρ Oph, is catalogued as a single B2III/B2IV star (C-ionizing, Houk & Smith-Moore 1988), with $T_{\text{eff}} \approx 23\,000$ K (Bondar 2012). This star is heating and dissociating gas layers creating an H II region of ~ 6 arcmin towards the PDR traced by the free–free continuum in the Parkes–MIT–NRAO (PMN) 4.85 GHz map, and by the H α emission in SHASSA (Casassus et al. 2008). In Fig. 3(a) we show normalized emission profiles for the IR templates and the

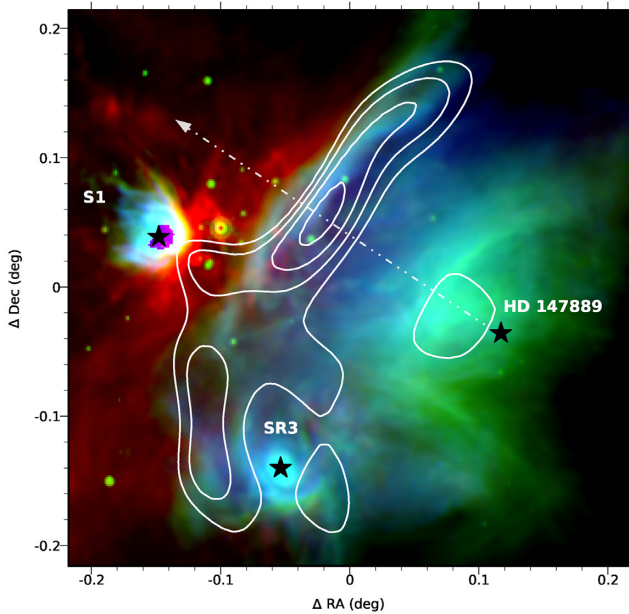


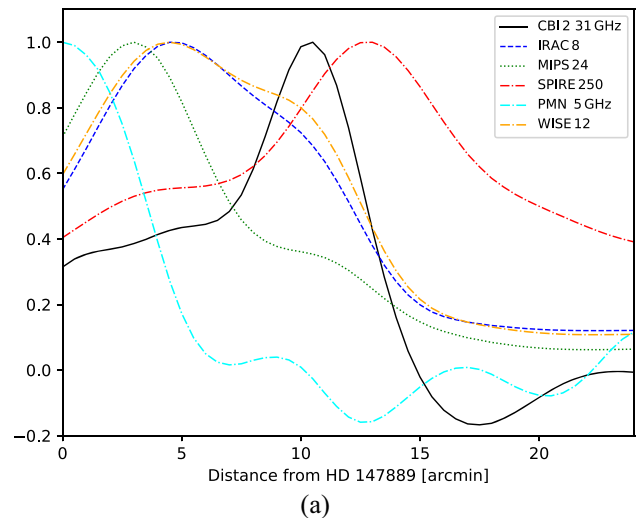
Figure 2. Overview of ρ Oph. Red: SPIRE 250 μm , green: MIPS 24 μm , blue: IRAC 8 μm (PDR). The centre of the image is at RA 16:25:55.20, Dec. -24:25:48.0 (J2000). The markers indicate the locations of the three early-type stars in the field. Contours follow a gpu-uvmem model of the 31 GHz continuum measured by the CBI2, at 30 per cent, 50 per cent, 70 per cent, and 90 per cent of the emission peak at $0.51 \text{ Jy beam}^{-1}$. The white-dashed arrow indicates the direction of the cut used to construct the emission profiles of the templates.

31 GHz data, for a cut starting from HD 147889 and passing through the 31 GHz emission peak, as shown by the dashed arrow in Fig. 2. We also plot the emission profile from the PMN 4.85 GHz map as a tracer of the free-free emission throughout the region. We find that, indeed, most of the 4.85 GHz emission comes from the vicinity of HD 147889. The 24 μm map in Fig. 2 also shows thermal emission from hot grains near HD 147889. Towards the PDR (at ~ 6 arcmin in Fig. 3) and through the peak of the 31 GHz emission, the 4.85 GHz emission decreases, reaching the noise level of the original map. This lack of free-free emission at the location of the PDR can also be seen in the 1.4 GHz and $\text{H}\alpha$ maps of ρ Oph presented in Planck Collaboration (2011).

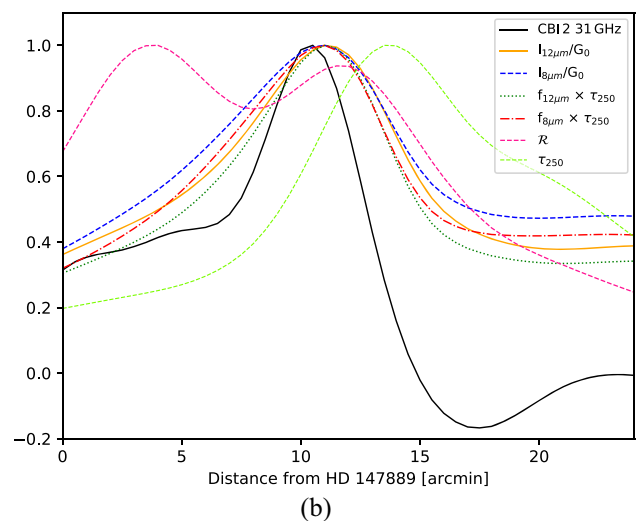
An interesting aspect of Fig. 2 is that the 31 GHz contours fall in the transition between small hot grains and bigger colder grains (reflected in the layered structure of the IR tracers, as also seen in Fig. 3a). This transition occurs at the PDR, where neutral Hydrogen becomes molecular. Deeper into the molecular core, away from HD 147889 in Fig. 2, the UV radiation field is attenuated, and the emergent emission progressively shifts towards 250 μm .

Fig. 3(a) shows that IRAC 8 μm and WISE 12 μm have a wider radial profile than that at 31 GHz, ranging from their peak at ~ 5 arcmin distance from HD 147789 up to ~ 15 arcmin. Note that around 5 arcmin there is a slight hump on the 31 GHz profile that matches the peak of IRAC 8 μm . Also, at ~ 10 arcmin, the WISE 12 μm profile shows a hump at the position of the 31 GHz peak. This correlations might imply a relation between the rotational excitation of dust grains that originate the SD emission and the vibrational states of the small grains seen in the 8 and 12 μm profiles.

We note that the most conspicuous feature in the IR-map in Fig. 2, the circumstellar nebula around S1, shows a very faint 31 GHz counterpart. This is particularly interesting as *Spitzer* IRS



(a)



(b)

Figure 3. Normalized emission profiles versus distance to ionizing star HD 147889. The profile cut, as shown by the dashed arrow in Fig. 2, was extracted starting from star HD 147889 and crossing the 31 GHz emission peak.

spectroscopy shows very bright PAHs bands in the nebulae around S1 and SR3, as well as in the ρ Oph W PDR (Habart et al. 2003; Casassus et al. 2008). This means that PAHs are not depleted around S1 and SR3, thus making the faint 31 GHz emission intriguing. Motivated by this, we performed a correlation analysis in order to quantify the best tracer of the 31 GHz emission throughout the region.

4 CORRELATION ANALYSIS

We study the morphological correlation between the 31 GHz data and different IR maps that trace PAHs and VSGs. In order to avoid biases due to image reconstruction, we performed the correlations in the visibility (uv) plane. To transform our data set to the uv -plane we used the MOCKCBI software from the CBI software tools. This program calculates the visibilities by Fourier-transforming a supplied map of the sky emission, in this case, various IR templates. To do this, all templates were reprojected to a 1024×1024 grid. In case that any of the original templates were of a smaller size, a noise gradient, calculated with the RMS noise limits of each map,

was added to the borders. This is an important step to consider, otherwise, the resulting visibility maps would show an abrupt step towards its borders, producing artefacts in the mock visibilities. To visualize and compare the trend of our results, we also calculated the correlations in the plane of the sky. We smoothed all the templates to 4.5 arcmin in order to fit CBI 2's angular resolution. All templates were re-gridded to ~ 3 pixels per beam to avoid correlated pixels.

4.1 PAH column density proxies

For the correlation analysis, we constructed proxies for the column density of PAHs. The mid-IR dust emission, due to PAHs, depends on the column density of the emitters and on the intensity of the local UV radiation, which can be quantified in units of the ISRF in the solar neighbourhood as the dimensionless parameter G_0 (Sellgren et al. 1985; Draine & Li 2007). If the observed 31 GHz emission corresponds to SD emission, a stronger correlation is expected with the mid-IR emission when divided by G_0 , as this will trace the column density of PAHs.

The radiation field intensity was estimated using the equation given by Ysard et al. (2010):

$$G_0 = (T_{\text{dust}}/17.5K)^{\beta_{\text{dust}}+4}. \quad (5)$$

This method derives from radiative equilibrium with a single grain size of $0.1 \mu\text{m}$ and an emissivity index¹ $\beta_{\text{dust}} = 2$, which is constant across the field. As β_{dust} may vary throughout the PDR, a constant β might not be a good approximation for G_0 . We estimated the impact of variable β_{dust} in equation (5). We created a map of β_{dust} and T_{dust} by fitting a modified blackbody to the far-IR data. For this, we used Herschel data at 100, 160, 250, 350, and 500 μm . This fit results in β_{dust} , τ , and T_{dust} maps that would let us identify variations in the PDR at 4.5 arcmin. The resulting G_0 map, calculated with the variable β_{dust} and T_{dust} maps from the fit, is morphologically equivalent to the G_0 estimation using a constant β_{dust} and Herschel's T_{dust} map. The Pearson correlation coefficient is $r = 0.95 \pm 0.02$ between both G_0 estimations. In this work, we are interested in comparing the morphology of the cm-wavelength (31 GHz) signal with that of the average radiation field along the line of sight. A 3D radiative transfer model that accounts for the IR spectral variations would provide an accurate estimation of the 3D UV radiation field ($G_0(\vec{x})$) and of the dust abundances (e.g. as in Galliano 2018). Such modelling is beyond the scope of this work.

In stochastic heating, we expect the intensity of the IR bands due to PAHs to be approximately proportional to both the UV field intensity and the PAH column, so that (as in Casassus et al. 2008)

$$\frac{I_{\nu \text{ PAH}}}{G_0} \propto N_{\text{PAH}}. \quad (6)$$

As templates for the PAHs emission, $I_{\nu \text{ PAH}}$, we used the WISE 12 μm and IRAC 8 μm intensity maps.

Another way to obtain a proxy for the column of PAHs, proposed by Hensley et al. (2016), is to correct $I_{\nu \text{ PAH}}$ by the dust radiance (\mathcal{R}) as a method to quantify the fraction of dust in PAHs (f_{PAH}). The dust radiance corresponds to the integrated intensity, $\mathcal{R} = \int_{\nu} I_{\nu}$. We calculated this expression by considering a modified blackbody as in Planck Collaboration XI (2014a, equation 10):

$$\mathcal{R} = \tau_{250} \frac{\sigma_S}{\pi} T_{\text{dust}}^4 \left(\frac{kT_{\text{dust}}}{h\nu_0} \right)^{\beta_{\text{dust}}} \frac{C(4 + \beta_{\text{dust}}) \zeta(4 + \beta_{\text{dust}})}{\Gamma(4) \zeta(4)}, \quad (7)$$

¹This is the spectral index of the grain opacity.

where τ_{250} is the optical depth at 250 μm , calculated using $\tau_{250} = I_{250 \mu\text{m}}/B_{250 \mu\text{m}}(T)$ by assuming an optically thin environment. Also, ν_0 is the frequency for 250 μm , σ_S is the Stefan-Boltzmann constant, k is the Boltzmann constant, h is the Planck constant, and Γ and ζ are the Gamma and Riemann-zeta functions, respectively. To recover the intensity units of the radiance map, we divide it by ν_0 , getting as a result \mathcal{R}/ν . Hence, the PAH fraction can be calculated as

$$\frac{\nu I_{\nu \text{ PAH}}}{\mathcal{R}} \propto f_{\text{PAH}}. \quad (8)$$

Thus, the product of the PAH fraction times the optical depth will be proportional to the PAH column density:

$$f_{\text{PAH}} \times \tau_{250} \propto N_{\text{PAH}}. \quad (9)$$

We note that Hensley et al. (2016) stress the need of a good correlation between the mid-IR map and \mathcal{R} , which is the case of our 4.5 arcmin $I_{\nu \text{ PAH}}$ and \mathcal{R} maps, with correlation coefficients $r > 0.6$. In Fig. 4, we show a close-up of the 31 GHz clean mosaic, along with the column density proxies constructed with WISE 12 μm and IRAC 8 μm , and the radiance map.

4.2 Pearson correlation analysis

Fig. 5 shows the scatter plots using the 31 GHz data and column density proxies $I_{12 \mu\text{m}}/G_0$ and $f_{12 \mu\text{m}} \cdot \tau_{250}$ in the plane of the sky. These scatter plots suggest a linear dependence between the CBI 2 data and each template, which justifies the use of the Pearson coefficient as a statistical measurement of the correlation. The Pearson correlation coefficient, r , provides a way to quantify and compare the degree of correlation between the 31 GHz signal and different templates, both in the uv -domain,

$$r_{uv} = \frac{\sum_k \omega_k (Vx_k - \bar{Vx})(Vy_k - \bar{Vy})}{\sqrt{\sum_k \omega_k (Vx_k - \bar{Vx})^2 \sum_k \omega_k (Vy_k - \bar{Vy})^2}}, \quad (10)$$

where ω_k is the weight for visibility datum V_k , and $\bar{Vx} = \sum_k \omega_k Vx_k / \sum_k \omega_k$ and $\bar{Vy} = \sum_k \omega_k Vy_k / \sum_k \omega_k$ are the weighted means of visibility data sets Vx and Vy , respectively, and in the sky-plane

$$r_{\text{sky}} = \frac{\sum_i (x_i - \bar{x})(y_i - \bar{y})}{\sqrt{\sum_i (x_i - \bar{x})^2 \sum_i (y_i - \bar{y})^2}}, \quad (11)$$

where \bar{x} and \bar{y} are the mean values of data sets x and y , respectively.

The correlations in the uv -plane (r_{uv}) are calculated for the entire visibility data set. On the other hand, the sky-plane cross-correlations are taken inside an area equivalent to half the mosaic's primary beam FWHM, shown as a dashed region in Fig. 4(a). This helps us avoid noisy outliers and measure the correlation within the area of interest, which is the PDR. We also masked the PMN galaxy identified in Fig. 1.

The uncertainties in r_{sky} were estimated with a Monte Carlo simulation. We added random Gaussian noise to the 31 GHz clean mosaic, before dividing by the mosaic attenuation map, with a dispersion given by the RMS noise of the 31 GHz clean mosaic. In each run of the simulations, the resulting 31 GHz intensity map is correlated with the corresponding template, and the final error in r_{sky} is the standard deviation of all the correlation coefficients. In the uv -plane, the r_{uv} errors are calculated under the same logic, but instead, we add random Gaussian noise to each visibility datum V_k using a dispersion given by its weight $\omega_k = 1/\sigma_k^2$, common to both the real and imaginary parts. We are interested in the relative

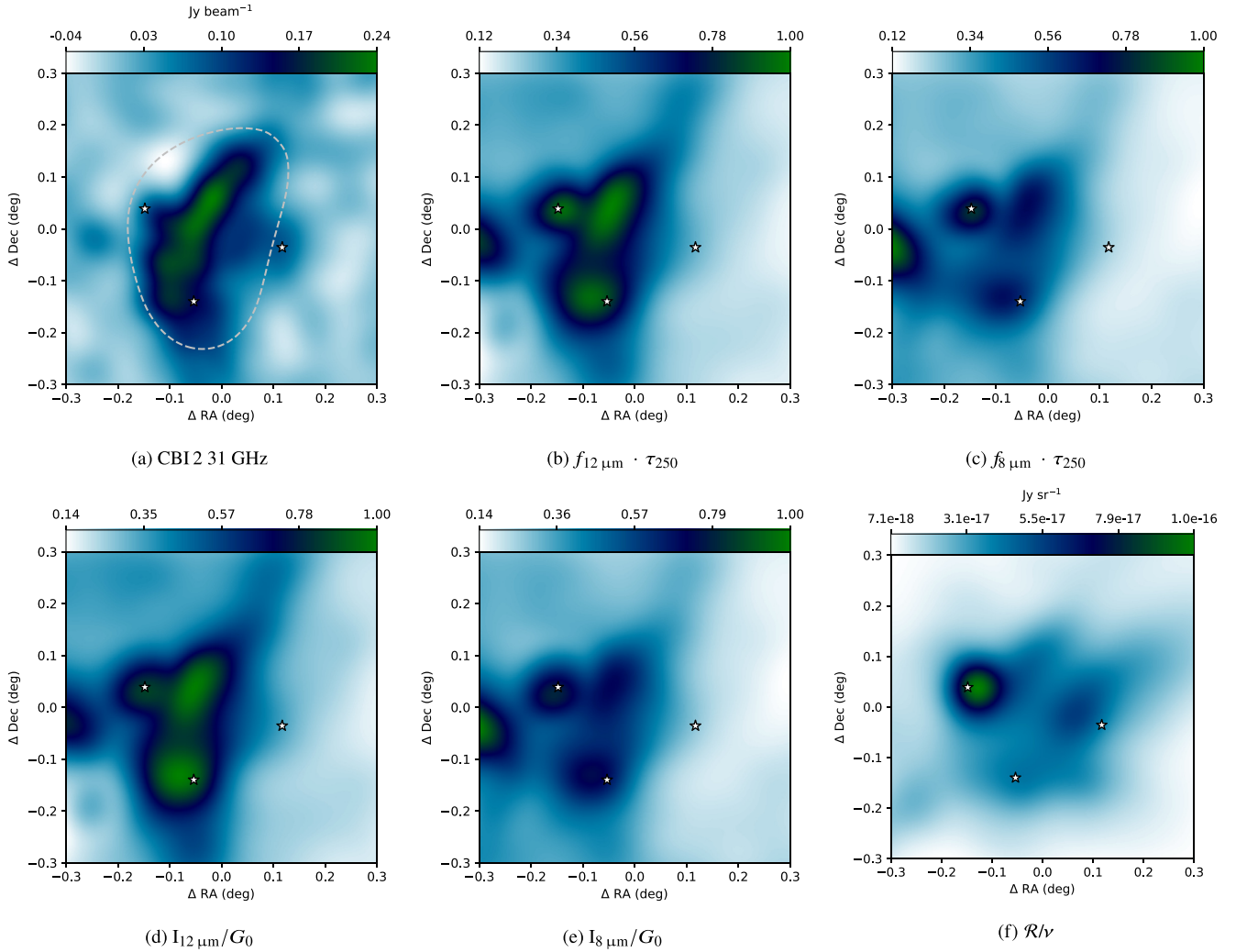


Figure 4. clean 31 GHz map (4a, close-up from Fig. 1), normalized proxies for PAHs column densities (4b–e) and radiance map (4f). The proxies for column densities correlate better with the 31 GHz data, and the morphology between them is very similar. In 4(a), the dashed region shows the area within which we calculated the plane of the sky correlations; it corresponds to 50 per cent of the mosaic’s primary beam. The position for the three early-type stars are also marked in each map.

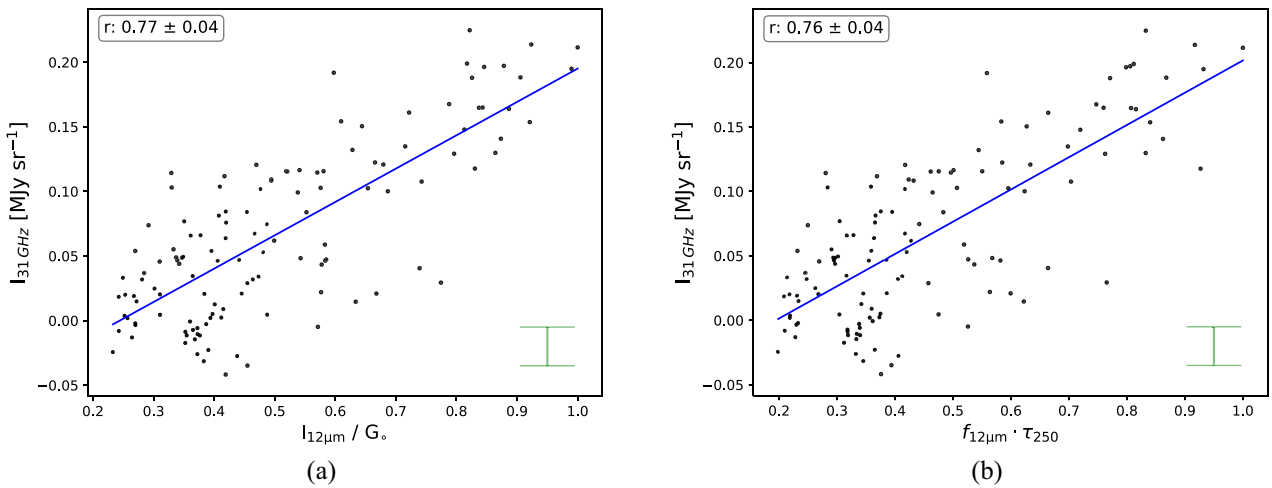


Figure 5. Linear correlations between the 31 GHz data and the column density proxies $I_{12\mu\text{m}}/G_0$ (5a) and $f_{12\mu\text{m}} \cdot \tau_{250}$ (5b), in the plane of the sky. RMS error bars (~ 0.03 MJy sr $^{-1}$) are shown for the 31 GHz data. The column density proxies axis (x -axis) are normalized in both cases and their errors are negligible.

Table 5. Pearson correlations between the 31 GHz data and different templates, for the plane of the sky (r_{sky}) and the uv -plane (r_{uv}).

Template	r_{uv}	r_{sky}
WISE 3	0.25 ± 0.01	0.61 ± 0.04
IRAC 8	0.26 ± 0.01	0.68 ± 0.04
WISE 12	0.29 ± 0.01	0.72 ± 0.04
WISE 22	0.15 ± 0.01	0.52 ± 0.04
MIPS 24	0.15 ± 0.01	0.51 ± 0.04
SPIRE 250	0.08 ± 0.01	0.40 ± 0.04
τ_{250}	-0.04 ± 0.01	0.11 ± 0.04
\mathcal{R}/ν	0.13 ± 0.01	0.51 ± 0.04
$f_{3\ \mu\text{m}}$	0.17 ± 0.01	0.23 ± 0.04
$f_{8\ \mu\text{m}}$	0.23 ± 0.01	0.32 ± 0.02
$f_{12\ \mu\text{m}}$	0.25 ± 0.01	0.37 ± 0.02
$f_{3\ \mu\text{m}} \cdot \tau_{250}$	0.27 ± 0.01	0.70 ± 0.04
$f_{8\ \mu\text{m}} \cdot \tau_{250}$	0.28 ± 0.01	0.59 ± 0.04
$f_{12\ \mu\text{m}} \cdot \tau_{250}$	0.34 ± 0.01	0.76 ± 0.04
$I_{3\ \mu\text{m}}/G_0$	0.29 ± 0.01	0.71 ± 0.04
$I_{8\ \mu\text{m}}/G_0$	0.26 ± 0.01	0.60 ± 0.04
$I_{12\ \mu\text{m}}/G_0$	0.34 ± 0.01	0.77 ± 0.04

variations of the Pearson coefficients between the templates, so any bias due to systematic errors will be the same for all the maps.

The resulting values for the correlations coefficients are listed in Table 5. We observe the same trends in both r_{sky} and r_{uv} , although the sky-plane results show higher correlations. This difference is expected, as the sky correlations were extracted within 50 per cent of the primary beam area, while the uv -plane correlations used all of the visibilities, which are integrated quantities over the whole primary beams.

Fig. 3(b) shows the cuts for the normalized radiance, τ_{250} , and column density proxies, starting from star HD 147889 and passing through the 31 GHz emission peak (as shown by the arrow in Fig. 2). Here, we see that the column density proxies of the small grains peak around the same location as the 31 GHz data. Note the shift of the IRAC 8 μm and WISE 12 μm profiles between Fig. 3(a) and their column density proxies in Fig. 3(b). It is also interesting to highlight that the location of the bump in the WISE 12 μm profile (at around 10 arcmin in Fig. 3a) matches the 31 GHz peak. This leads to a stronger correlation between both templates, which is also reflected in Fig. 3b, where $I_{12\ \mu\text{m}}/G_0$ and $f_{12\ \mu\text{m}} \cdot \tau_{250}$ are narrower and show a more similar profile to the 31 GHz data. As shown in Table 5, the best correlation is indeed with PAH column density proxy $I_{12\ \mu\text{m}}/G_0$. The role of the WISE 3 μm map as a tracer for smaller PAHs will be discussed in Section 5.

Note that, in Fig. 3(b), the radiance profile shows two peaks: one around 5 arcmin from HD 147889, which is related to hotter dust grains nearby the star, and a second one along the PDR but shifted ~ 2 arcmin from the 31 GHz profile, which is related to a larger optical depth (τ_{250}). The τ_{250} peak, which traces the concentration of big grains, is shifted towards the molecular cloud, matching the peak of SPIRE 250 μm (Fig. 3a) at ~ 13 arcmin. Table 5 shows that the τ_{250} map does not correlate with the 31 GHz map, while the correlation coefficient for the radiance template (\mathcal{R}) is moderate. Historically, sub-mm templates have been used to trace dust emission (Dickinson et al. 2018), but, in this case, the quantification of the sub-mm emission is better traced by the radiance in comparison with τ_{250} or the intensity at any given sub-mm frequency. This is consistent with the result by Hensley

Table 6. Pearson coefficients for the original visibility data set and the visibility data set using uv -tapering for an equivalent angular resolution of 13.5 arcmin (\sim three times the original CBI2 angular resolution). We show the ratio between the Pearson coefficients of the two data sets. In particular, we see that the dust radiance coefficient tends to increase the most at a lower equivalent angular resolution.

Template	r_{uv}	$r_{uv-13.5'}$	Ratio
WISE 3	0.25 ± 0.01	0.32 ± 0.02	1.3 ± 0.1
IRAC 8	0.26 ± 0.01	0.35 ± 0.02	1.3 ± 0.1
WISE 12	0.29 ± 0.01	0.37 ± 0.02	1.3 ± 0.1
WISE 22	0.15 ± 0.01	0.20 ± 0.01	1.4 ± 0.1
MIPS 24	0.15 ± 0.01	0.20 ± 0.02	1.3 ± 0.2
SPIRE 250	0.08 ± 0.01	0.09 ± 0.01	1.1 ± 0.2
τ_{250}	-0.04 ± 0.01	-0.06 ± 0.01	1.5 ± 0.4
\mathcal{R}/ν	0.13 ± 0.01	0.20 ± 0.02	1.5 ± 0.2
$f_{3\ \mu\text{m}}$	0.17 ± 0.01	0.21 ± 0.02	1.2 ± 0.1
$f_{8\ \mu\text{m}}$	0.23 ± 0.01	0.29 ± 0.02	1.3 ± 0.1
$f_{12\ \mu\text{m}}$	0.25 ± 0.01	0.31 ± 0.02	1.2 ± 0.1
$f_{3\ \mu\text{m}} \cdot \tau_{250}$	0.27 ± 0.01	0.34 ± 0.01	1.3 ± 0.1
$f_{8\ \mu\text{m}} \cdot \tau_{250}$	0.28 ± 0.01	0.37 ± 0.03	1.3 ± 0.1
$f_{12\ \mu\text{m}} \cdot \tau_{250}$	0.34 ± 0.01	0.42 ± 0.03	1.2 ± 0.1
$I_{3\ \mu\text{m}}/G_0$	0.29 ± 0.01	0.37 ± 0.03	1.3 ± 0.1
$I_{8\ \mu\text{m}}/G_0$	0.26 ± 0.01	0.34 ± 0.03	1.3 ± 0.1
$I_{12\ \mu\text{m}}/G_0$	0.34 ± 0.01	0.42 ± 0.03	1.2 ± 0.1

et al. (2016) where the radiance template is the best tracer for the AME.

4.3 Correlation analysis as a function of angular resolution

The cross-correlations also depend on angular resolution. We repeated the correlations in the uv -plane for an equivalent angular resolution of 13.5 arcmin, closer to the approximate maximum recoverable scale (\sim three times the CBI2 synthesized beam). To do this, we applied a uv -taper by multiplying the visibility weights with a Gaussian, $W = \exp(- (u^2 + v^2)/l^2)$. The results are presented in Table 6, where we also show the ratio between the Pearson coefficients of the original and the tapered data set. These correlations show the highest increase for \mathcal{R}/ν and τ_{250} , but note that the correlation for τ_{250} is very close to zero. We also calculated the correlations in the sky plane by smoothing the templates to angular resolutions of 9 and 13.5 arcmin and observed the same tendency: the Pearson coefficient of the dust radiance maps increases the most at lower angular resolutions, while the column density proxies tend to remain equal.

The fact that the radiance template shows the highest relative increase in its Pearson coefficient could explain the results obtained by Hensley et al. (2016), where their dust radiance template correlated the best with their AME template at an angular resolution of 1° . Based on their correlation results, they concluded that PAHs might not be responsible for the AME. This is not the case for our 4.5 arcmin maps, so we believe that PAHs cannot be ruled out as possible SD carriers. In this PDR, the 8 and 12 μm bands are dominated by PAHs (see e.g. Habart et al. 2003; Draine & Li 2007; Compiègne et al. 2011), so the fact that we found a good correlation between these bands and the 31 GHz emission indicates that the PAHs might be important AME emitters.

4.4 AME correlation slopes

Typically, AME emissivities have been quantified with correlation slopes in terms of IR emission (e.g. $I_{30\ \text{GHz}} / I_{100\ \mu\text{m}}$) or using an

Table 7. AME correlation slopes for ρ Oph W between typical AME frequencies and dust templates. The τ_{353} map can be considered a better dust template as it traces the dust column density. We find that most of the ρ Oph 31 GHz flux must be coming from ρ Oph W.

Frequency (GHz)	Angular resolution	Correlation slope	Units	Template	Reference
31	4.5 arcmin	15.5 ± 0.2	$10^6 \mu\text{K}$	τ_{353}	This work.
22.8	1°	23.9 ± 2.3	$10^6 \mu\text{K}$	τ_{353}	Dickinson et al. (2018)
31	4.5 arcmin	2.18 ± 0.04	$\mu\text{K}/(\text{MJy sr}^{-1})$	100 μm (IRIS)	This work.
22.8	1°	8.3 ± 1.1	$\mu\text{K}/(\text{MJy sr}^{-1})$	100 μm (IRIS)	Dickinson et al. (2018)

optical depth map ($I_{30\text{GHz}} / \tau_{353\text{GHz}}$; see Dickinson et al. 2018). We calculated the correlation slope between our 31 GHz data, and τ_{353} and IRIS 100 μm . For this, we measured the mean emission within the PDR filament using intensities larger than 15σ (as the contour defined in Fig. 1) in the primary beam corrected clean map. The original angular resolutions for the τ_{353} and IRIS 100 μm maps (5 and 4.3 arcmin, respectively) are very similar to CBI2's angular resolution of 4.5 arcmin. In Table 7, we list the values for the AME correlation slopes. We also show the correlation slopes measured with the same templates by Dickinson et al. (2018), at an angular resolution of 1° . We find that a large fraction of the AME correlation slope measured in ρ Oph on scales of 1° must be coming from the ρ Oph W PDR. This is especially evident when using the τ_{353} map, where the AME correlation slope of the 4.5 arcmin ρ Oph W PDR observations is ~ 65 per cent of the AME correlation slope of the 1° ρ Oph observations. ρ Oph W shows the highest AME emissivity in terms of the τ_{353} map, which is considered as a very reliable dust template as it traces the dust column density (Dickinson et al. 2018). These emissivities are about a factor 2–3 higher than other values measured at high Galactic latitudes and also in Perseus, the brightest AME source in the sky according to Planck Collaboration (2011). A possible explanation for the larger slope in ρ Oph W could be found in the finer linear resolution in this work, of ~ 0.2 pc, compared to ~ 2.3 pc in Planck Collaboration (2011). The fact that ρ Oph is closer to us means that we can resolve the AME from the PDR. When integrated in the telescope beam (e.g. Planck analysis over 1° scales), there is proportionally a larger amount of AME coming from the high density and excited PDR compared to the emission from the regions that have lower emissivities, i.e. AME from the denser cores, or from the more diffuse gas.

4.5 Spectral index

The wide frequency coverage of the CBI2 correlator, between 26 and 36 GHz, may place constraints on the spectral properties of the 31 GHz signal. We split the visibilities (V) in two sub-sets: one for the low-frequency channels (6–10) centred at 28.5 GHz, and one for the high-frequency channels (1–5) centred at 33.5 GHz. We then calculated the correlation slopes ($a^{\text{High}}, a^{\text{Low}}$) between the two sub-sets and the mock visibilities for $I_{12\mu\text{m}}/G_0$ (the best-correlated proxy), following

$$V_{31\text{GHz}}^{\text{High/Low}} = a^{\text{High/Low}} V_{12\mu\text{m}/G_0}. \quad (12)$$

Note that $\log(a^{\text{High}}/a^{\text{Low}})$ is proportional to the spectral index α . We obtained a spectral index of $\alpha = 0.05 \pm 0.08$, which indicates a flat spectrum. However, we must also take into account the difficulty of obtaining a reliable spectral index due to any possible calibration and systematic errors. The spectral index measured between the low and high-frequency channel is none the less consistent with the shape of the ρ Oph spectrum in Planck Collaboration (2011).

5 QUALITATIVE ANALYSIS OF THE PAH SIZES

The results in Table 5 show that column density proxies of PAH tracers at 3, 8 and 12 μm correlate the best with the 31 GHz emission. Note that, in particular, the 3 μm band is dominated by the smallest PAHs (sizes ~ 0.4 nm), which are the most prone to destruction by UV radiation, while the 8 and 12 μm bands, in comparison, are dominated by bigger PAHs. Given this, a good tracer of the PAH sizes is the 12 $\mu\text{m}/3 \mu\text{m}$ ratio map (Allamandola, Tielens & Barker 1985; Ricca et al. 2012; Croiset et al. 2016). To construct it, we removed the point sources in the WISE 3 μm map, and smoothed both the WISE 12 and 3 μm maps to CBI2's angular resolution. In Fig. 6(a) we show the 4.5 arcmin map for the 12 $\mu\text{m}/3 \mu\text{m}$ ratio, along with the 31 GHz contours (same contours as in Fig. 1). At this angular resolution, it is interesting to note the increment of the ratio in the transition between the PDR and the molecular cloud to the East in Fig. 6(a). This is also seen in Fig. 6(b), where we show the normalized emission profiles for the cut in Fig. 2 versus the distance to the ionizing star HD 147889. Here, the minimum of the 12 $\mu\text{m}/3 \mu\text{m}$ ratio is aligned with the PDR surface (defined by the first black vertical line, ~ 6 arcmin in Fig. 6b), while the peak of the ratio occurs at the transition between the PDR and the molecular cloud (defined by the second black vertical line, ~ 14 arcmin in Fig. 6b). This peak might be an indication that the PAHs size increases in the PDR towards the molecular cloud.

The 3 $\mu\text{m}/8 \mu\text{m}$ ratio map can also give us an indication of the contribution of the smallest PAHs. We calculated the plane of the sky correlation between the 3 $\mu\text{m}/8 \mu\text{m}$ ratio and the 31 GHz emission, and obtained a Pearson coefficient of $r_{\text{sky}} = -0.21 \pm 0.03$. The low value of the anticorrelation indicates that the smallest grains do not necessarily correlate better with the 31 GHz map, as it can also be seen in Table 5, where the correlation in WISE 3 is not better than with IRAC 8. Fig. 6(b) also shows the normalized profile for the 3 $\mu\text{m}/8 \mu\text{m}$ ratio. The behaviour of this template is similar to the 12 $\mu\text{m}/3 \mu\text{m}$ map, but shifted towards the interior of the molecular cloud. Overall, these ratios reveal a factor of ~ 1.5 variation in the size of the emitting PAHs throughout the ρ Oph W PDR.

6 EMISSIVITY VARIATIONS

In our correlation analysis (Section 4) we found that the 31 GHz map correlates best with $I_{12\mu\text{m}}/G_0$, a template for the PAH column density. Also, we note that there is significant scatter about the linear cross-correlations between the 31 GHz emission and the PAH column density proxies, as shown in Fig. 5. Motivated by this, we study the possibility that this scatter is produced by SD emissivity variations along the PDR.

In order to assess the extent to which the physical mechanisms leading to the 31 GHz emission depend on the local environment, we tested for the hypothesis that the emergent 31 GHz intensity is *only* proportional to the column of the emitters, i.e. N_{PAH} . We

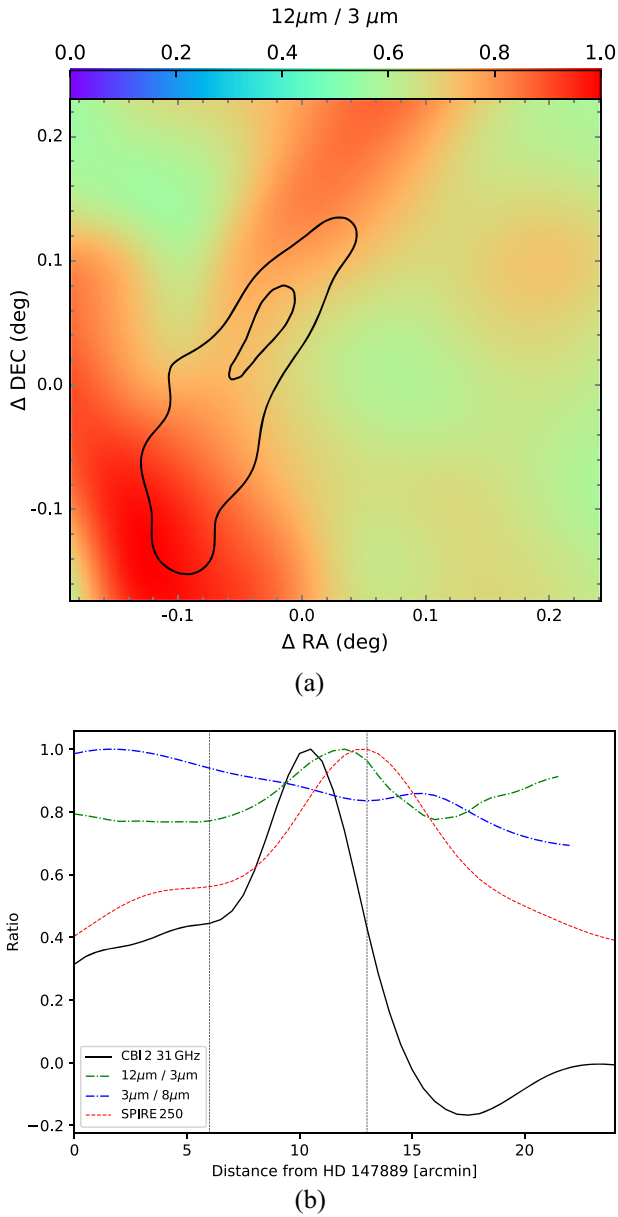


Figure 6. 6a: Normalized $12\ \mu\text{m}/3\ \mu\text{m}$ ratio in the ρ Oph W PDR. 6b: normalized emission profiles versus distance to ionizing star HD 147889 for the $12\ \mu\text{m}/3\ \mu\text{m}$ and $3\ \mu\text{m}/8\ \mu\text{m}$ ratios in comparison to the 31 GHz and 250 μm emission. The profile cut corresponds to the dashed arrow in Fig. 2 and the black vertical lines define the PDR.

construct a proxy that will let us measure any emissivity variation in the PDR as in Casassus et al. (2008), and define the 31 GHz emissivity per SD emitter (i.e. PAHs in our hypothesis), \hat{j}_v , which should be proportional to the SD emissivity per H-nucleus for a fixed grain population:

$$\hat{j}_v \equiv \frac{I_v(31\text{GHz})}{N_{\text{PAH}}} \propto j_v \equiv \frac{I_v}{N_H}. \quad (13)$$

Using equation (6), we can propose a proxy for \hat{j}_v :

$$\hat{j}_v^{\text{proxy}} \equiv \frac{I_v(31\text{GHz})}{I_{12\ \mu\text{m}}/G_0}. \quad (14)$$

The `gpu-uvmem` model images for $I_v^{\text{uvmem}}(31\text{GHz})$ and $I_{12\ \mu\text{m}}^{\text{uvmem}}/G_0$ provide a finer angular resolution than the `clean`

mosaic, and may pick up larger variations in emissivity. Fig. 7 shows $I_v^{\text{uvmem}}(31\text{GHz})$ (Fig. 7a), as well as the normalized \hat{j}_v^{proxy} map defined in equation (14) (Fig. 7b), along with its noise map (Fig. 7c). As explained in Section 3, the bulk of the free-free emission is located around HD 147889. Given this, we masked a region with a radius of 6 arcmin around HD 147889 in the `gpu-uvmem` maps, in order to quantify only the SD component using \hat{j}_v^{proxy} . Note that the \hat{j}_v^{proxy} map (Fig. 7b) shows variations throughout the region, with a peak that matches the peak at 31 GHz in the ρ Oph W PDR.

In Table 8, we list \hat{j}_v^{proxy} variations for different locations in the region. We found that the \hat{j}_v^{proxy} map has a peak that is 25 times higher than the 3σ noise. We repeated this calculation on a `clean` \hat{j}_v^{proxy} map and found an emissivity peak 10 times stronger than its 3σ noise. This difference is expected, as the `gpu-uvmem` map resolves much better the CBI 2 morphology.

Interestingly, the emissivity variation between the \hat{j}_v^{proxy} peak and the location of S1 is 22.8, very close to the strongest variation in ρ Oph W at 3σ . The fact that there is no significant 31 GHz emission originating at S1 (as seen in Figs 1 and 2) implies that the radio-emission mechanism is enhanced by the local conditions in the PDR, otherwise, we would see higher levels of 31 GHz emission near S1, given its large column of small grains (i.e. PAHs; Casassus et al. 2008).

The nature of the SD emissivity variations in ρ Oph may rely on various scenarios. SD models predict peak frequencies in the range 50–90 GHz for the typical environmental conditions of a PDR (e.g. Draine & Lazarian 1998a; Ysard, Juvela & Verstraete 2011; Hensley & Draine 2017a). However, only one reported observation of the California nebula is consistent with a SD spectrum with a (50 ± 17) GHz peak (Planck Collaboration XV 2014c). It is clear that the frequency of the SD spectrum must be changing due to environmental conditions across the PDR. In this case, the observed emissivity variations could be associated with a shift in the peak frequency. Nevertheless, the analysis in this work is based on the assumption that the 31 GHz emission maps the AME.

A tentative explanation for the local emissivity boost, in the SD paradigm, could be that the main spin-up mechanism in ρ Oph W are ion collisions (Draine & Lazarian 1998b). The electromagnetic coupling between passing C^+ ions and the grain dipole moment impart torques on the grain. As the rotational excitation by ions is more effective for charged grains (Hensley & Draine 2017a), a possible explanation could be that the PDR is hosting preferentially charged PAHs spun-up by C^+ . As observed in Fig. 7, the fainter signal from S1 and SR3 in the radio maps of ρ Oph could then be naturally explained by the fact that these stars are too cold to create conspicuous C II regions (Casassus et al. 2008). In addition to the rotational excitation of charged grains, we could also add the effect of a possible changing penetration of the ISRF through the PDR due to the morphology of the cloud. The variations in the ISRF intensity affect the grain size distribution and, most likely, their dipole moment, and these factors can produce considerable changes in the SD emissivity (Hoang, Lazarian & Draine 2011). Thus, further analysis of the PDR spectrum at different radio frequencies is required to calculate its physical parameters and understand the causes of the detected SD emissivity variations.

7 CONCLUSIONS

We report 31 GHz observations from CBI 2 of the ρ Oph W PDR, at an angular resolution of 4.5 arcmin. The emission runs along the PDR exposed to the ionizing star HD 147889. Interestingly, there is

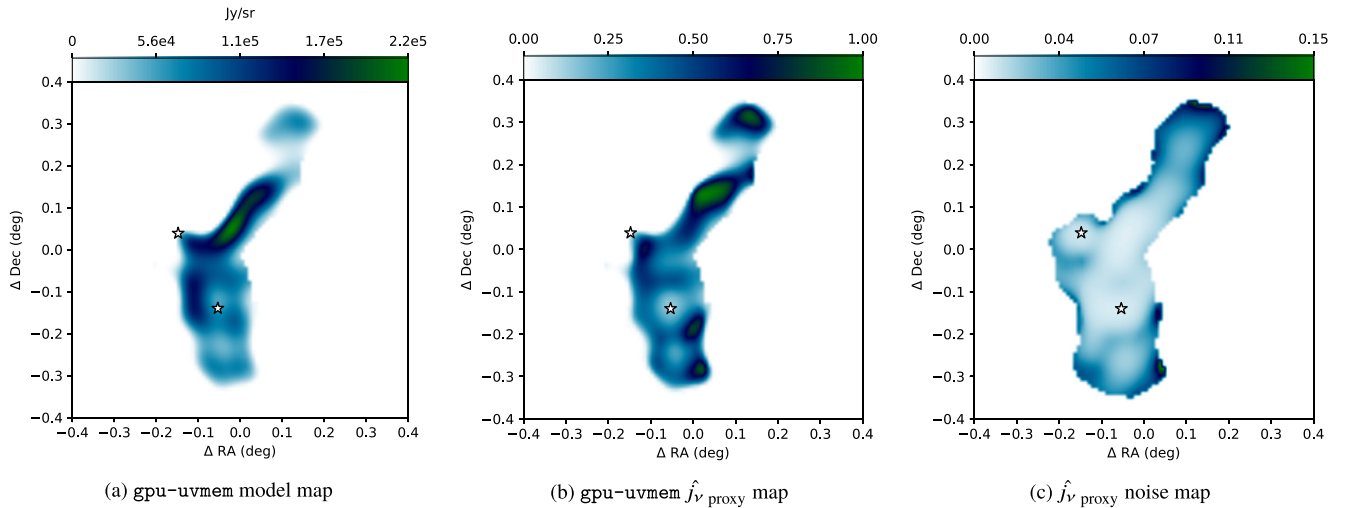


Figure 7. 7a: CBI 2 31 GHz gpu-uvmem model image. 7b: normalized \hat{j}_v^{proxy} map (with a peak of 2.19 ± 0.04 , in arbitrary units) and 7c: \hat{j}_v^{proxy} – normalized noise map (the scale corresponds to that of Fig. 7b). We used a mask around HD 147889 in order to avoid the bulk of the free-free emission. The observed blob towards the northern part of the filament is detected at 3σ over the noise in the CBI 2 clean map and could be the continuation of the PDR emission (no catalogued source was identified in that position).

Table 8. Emissivities variations in ρ Oph measured with the \hat{j}_v^{proxy} map.

Ratio	R
$S/N_{\text{Peak at } 3\sigma}$ ^a	25.6
$\hat{j}_v^{\text{proxy}} - \text{Peak} / \hat{j}_v^{\text{proxy}} - S1$ ^b	22.8 ± 5.2
$\hat{j}_v^{\text{proxy}} - \text{Peak} / \hat{j}_v^{\text{proxy}} - SR3$ ^c	6.2 ± 0.3

^a Ratio between the emissivity peak and its 3σ noise.

^b Ratio between the peak and at the location of S1.

^c Ratio between the peak and at the location of SR3.

no significant 31 GHz emission from S1, the brightest IR nebula in the complex.

To understand the nature of the 31 GHz emission, we calculated the correlations of the CBI 2 data with different IR templates, with PAHs column density proxies, and with dust radiance and optical depth templates. We show that the 31 GHz emission is related to the local PAH column density. The best correlation was found when using the $12 \mu\text{m}$ PAH column density proxy and it is significantly better than when using the 8 and $3 \mu\text{m}$ PAH column density proxies.

We also measured the correlations at different angular resolutions and found that the dust radiance correlation is better at lower angular resolution. This shows that the effect of angular resolution must be considered when interpreting morphological correlations, implying in this case that PAHs cannot be ruled out as SD carriers, as previous studies at lower angular resolutions have suggested. Additionally, we calculated a spectral index of $\alpha = 0.05 \pm 0.08$, between 28.5 and 33.5 GHz, that is consistent with the flat spectrum previously reported on this region. Using a $12 \mu\text{m} / 3 \mu\text{m}$ ratio map, we measured an increase of the PAH size in the transition between the PDR and the molecular cloud.

Motivated by the intrinsic scatter in the correlation plots, we constructed a proxy for the 31 GHz emissivity per SD emitter so as to quantify its variations. Using a gpu-uvmem model of the 31 GHz emission, we found that the SD emissivity peak over the PDR is, at least, 25 times greater over the noise, at 3σ , and 23 times greater than at the location of star S1, also at 3σ .

The SD emissivity boost in ρ Oph W appears to be dominated by local conditions in the PDR. Based on the fainter 31 GHz signal from stars S1 and SR3, possible explanations are environmental ions or a changing grain population. In the framework of the SD interpretation, these emissivity variations may hold the key to identify the dominant grain spin-up mechanisms. Further multirequency radio analysis of the PDR spectrum is needed in order to better understand the conditions that give rise to SD.

ACKNOWLEDGEMENTS

We thank the anonymous referee for helpful comments. CAT and SC acknowledge support from FONDECYT grant 1171624. MV acknowledges support from FONDECYT through grant 11191205. This work used the Brella cluster (FONDEQUIP project EQM140101) hosted at DAS/U. de Chile. MC acknowledges support granted by CONICYT PFCHA/DOCTORADO BECAS CHILE/2018 - 72190574. CD was supported by an ERC Starting (Consolidator) grant (307209) under the FP7 and an STFC Consolidated grant (ST/P000649/1). This work was supported by the Strategic Alliance for the Implementation of New Technologies (SAINT, see www.astro.caltech.edu/chajnantor/saint/index.html), and we are most grateful to the SAINT partners for their strong support. We gratefully acknowledge support from B. Rawn and S. Rawn Jr. The CBI was supported by NSF grants 9802989, 0098734, and 0206416. This research has used data from the Herschel Gould Belt survey project (<http://gouldbelt-herschel.cea.fr>).

REFERENCES

- Ali-Haïmoud Y., Hirata C. M., Dickinson C., 2009, *MNRAS*, 395, 1055
 Allamandola L. J., Tielens A. G. G. M., Barker J. R., 1985, *ApJ*, 290, L25
 Ami Consortium, 2009, *MNRAS*, 394, L46
 André P. et al., 2010, *A&A*, 518, L102
 Battistelli E. S. et al., 2015, *ApJ*, 801, 111
 Battistelli E. S. et al., 2019, *ApJ*, 877, L31
 Bennett C. L. et al., 2013, *ApJS*, 208, 20
 Bondar A., 2012, *MNRAS*, 423, 725

- Cárcamo M., Román P. E., Casassus S., Moral V., Rannou F. R., 2018, *Astron. Comput.*, 22, 16
- Casassus S., Cabrera G. F., Förster F., Pearson T. J., Readhead A. C. S., Dickinson C., 2006, *ApJ*, 639, 951
- Casassus S. et al., 2008, *MNRAS*, 391, 1075
- Castellanos P. et al., 2011, *MNRAS*, 411, 1137
- Compiègne M. et al., 2011, *A&A*, 525, A103
- Condon J. J., Cotton W. D., Greisen E. W., Yin Q. F., Perley R. A., Taylor G. B., Broderick J. J., 1998, *AJ*, 115, 1693
- Croiset B. A., Candian A., Berné O., Tielens A. G. G. M., 2016, *A&A*, 590, A26
- Davies R. D., Dickinson C., Banday A. J., Jaffe T. R., Górski K. M., Davis R. J., 2006, *MNRAS*, 370, 1125
- Dickinson C., Davies R. D., Bronfman L., Casassus S., Davis R. J., Pearson T. J., Readhead A. C. S., Wilkinson P. N., 2007, *MNRAS*, 379, 297
- Dickinson C. et al., 2009, *ApJ*, 690, 1585
- Dickinson C. et al., 2018, *New Astron. Rev.*, 80, 1
- Draine B. T., Lazarian A., 1998a, *ApJ*, 494, L19
- Draine B. T., Lazarian A., 1998b, *ApJ*, 508, 157
- Draine B. T., Li A., 2007, *ApJ*, 657, 810
- Erickson W. C., 1957, *ApJ*, 126, 480
- Fazio G. G. et al., 2004, *ApJS*, 154, 10
- Finkbeiner D. P., 2004, *ApJ*, 614, 186
- Gaia Collaboration, 2018, *A&A*, 616, A1
- Galliano F., 2018, *MNRAS*, 476, 1445
- Génova-Santos R. et al., 2015, *MNRAS*, 452, 4169
- Griffin M. J. et al., 2010, *A&A*, 518, L3
- Griffith M. R., Wright A. E., Burke B. F., Ekers R. D., 1994, *ApJS*, 90, 179
- Habart E., Boulanger F., Verstraete L., Pineau des Forêts G., Falgarone E., Abergel A., 2003, *A&A*, 397, 623
- Healey S. E., Romani R. W., Taylor G. B., Sadler E. M., Ricci R., Murphy T., Ulvestad J. S., Winn J. N., 2007, *ApJS*, 171, 61
- Hensley B., Murphy E., Staguhn J., 2015, *MNRAS*, 449, 809
- Hensley B. S., Draine B. T., 2017a, *ApJ*, 836, 179
- Hensley B. S., Draine B. T., 2017b, *ApJ*, 834, 134
- Hensley B. S., Draine B. T., Meisner A. M., 2016, *ApJ*, 827, 45
- Hoang T., Lazarian A., Draine B. T., 2011, *ApJ*, 741, 87
- Hoang T., Vinh N.-A., Quynh Lan N., 2016, *ApJ*, 824, 18
- Houk N., Smith-Moore M., 1988, Michigan Catalogue of Two-dimensional Spectral Types for the HD Stars. Volume 4, Declinations -26.0 to -12.0. Department of Astronomy, University of Michigan, Ann Arbor, MI
- Kogut A., Banday A. J., Bennett C. L., Gorski K. M., Hinshaw G., Reach W. T., 1996, *ApJ*, 460, 1
- Ladjelate B., et al., 2020, *A&A*, preprint ([arXiv:2001.11036](https://arxiv.org/abs/2001.11036))
- Leitch E. M., Readhead A. C. S., Pearson T. J., Myers S. T., 1997, *ApJ*, 486, L23
- Liseau R. et al., 1999, *A&A*, 344, 342
- McMullin J. P., Waters B., Schiebel D., Young W., Golap K., 2007, in Shaw R. A., Hill F., Bell D. J., eds, in ASP Conf. Ser. Vol. 376, Astronomical Data Analysis Software and Systems XVI. Astron. Soc. Pac., San Francisco. p. 127
- Meisner A. M., Finkbeiner D. P., 2014, *ApJ*, 781, 5
- Murphy E. J. et al., 2010a, *ApJ*, 709, L108
- Murphy E. J., Linden S. T., Dong D., Hensley B. S., Momjian E., Helou G., Evans A. S., 2018, *ApJ*, 862, 20
- Murphy T. et al., 2010b, *MNRAS*, 402, 2403
- Nolan P. L. et al., 2012, *ApJS*, 199, 31
- Padin S. et al., 2002, *PASP*, 114, 83
- Pearson T. J. et al., 2003, *ApJ*, 591, 556
- Pilbratt G. L. et al., 2010, *A&A*, 518, L1
- Pillari P., Montillaud J., Berné O., Joblin C., 2012, *A&A*, 542, A69
- Planck Collaboration XX, 2011, *A&A*, 536, A20
- Planck Collaboration XII, 2013, *A&A*, 557, A53
- Planck Collaboration XI, 2014a, *A&A*, 571, A11
- Planck Collaboration XII, 2014b, *A&A*, 571, A12
- Planck Collaboration XV, 2014c, *A&A*, 565, A103
- Planck Collaboration XXV, 2015, *A&A*, 582, A28
- Readhead A. C. S. et al., 2004a, *Science*, 306, 836
- Readhead A. C. S. et al., 2004b, *ApJ*, 609, 498
- Ricca A., Bauschlicher Charles W. J., Boersma C., Tielens A. G. G. M., Allamandola L. J., 2012, *ApJ*, 754, 75
- Rieke G. H. et al., 2004, *ApJS*, 154, 25
- Scaife A. M. M. et al., 2010a, *MNRAS*, 403, L46
- Scaife A. M. M. et al., 2010b, *MNRAS*, 406, L45
- Sellgren K., Allamandola L. J., Bregman J. D., Werner M. W., Wooden D. H., 1985, *ApJ*, 299, 416
- Sowards-Emmerd D., Romani R. W., Michelson P. F., Ulvestad J. S., 2004, *ApJ*, 609, 564
- Taylor A. C. et al., 2011, *MNRAS*, 418, 2720
- Tibbs C. T. et al., 2011, *MNRAS*, 418, 1889
- Tibbs C. T., Scaife A. M. M., Dickinson C., Paladini R., Davies R. D., Davis R. J., Grainge K. J. B., Watson R. A., 2013, *ApJ*, 768, 98
- Tibbs C. T. et al., 2016, *MNRAS*, 456, 2290
- Tielens A. G. G. M., 2008, *ARA&A*, 46, 289
- Vidal M. et al., 2011, *MNRAS*, 414, 2424
- Vidal M., Dickinson C., Harper S. E., Casassus S., Witt A. N., 2020, *MNRAS*, 495, 1122
- Watson R. A., Rebolo R., Rubiño-Martín J. A., Hildebrandt S., Gutiérrez C. M., Fernández-Cerezo S., Hoyland R. J., Battistelli E. S., 2005, *ApJ*, 624, L89
- Wright E. L. et al., 2010, *AJ*, 140, 1868
- Ysard N., Miville-Deschênes M. A., Verstraete L., 2010, *A&A*, 509, L1
- Ysard N., Juvela M., Verstraete L., 2011, *A&A*, 535, A89

This paper has been typeset from a $\text{\TeX}/\text{\LaTeX}$ file prepared by the author.